Materials Advances

ROYAL SOCIETY OF CHEMISTRY

PAPER

View Article Online
View Journal | View Issue



Cite this: *Mater. Adv.*, 2023, 4, 223

# A non-covalent supramolecular dual-network polyelectrolyte evaporator based on direct-ink-writing for stable solar thermal evaporation†

Sihan Tang,[a] Xinyue Lu,[a] Peng Geng,[a] Daobing Chen,[a] Yunsong Shi,[c] Jin Su,[a] Yan Zhou,*[b] Bin Su *[a] and Shifeng Wen *[a]

Polymers possessing highly adjustable physicochemical properties have been accepted as ideal flexible materials for solar thermal evaporation, which is considered as an eco-friendly and progressive strategy for water reclamation. Conventional dual-network polymers based on the construction of covalent and non-covalent interactions usually involve toxic reactive monomers, initiators and organic solvents in 3D printing. The integration of additive manufacturing into the construction of supramolecular non-covalent dual-networks to achieve structural and performance optimisation remains a noteworthy part. Here we developed a 3D-printed anti-swelling polyelectrolyte evaporator consisting of k-carrageenan (CG), poly(diallyldimethylammoniumchloride) (PDADMAC), and carbon nanotubes (CNTs). CG-PDADMAC-CNT (CGP-CNT) was constructed by non-covalent supramolecular interactions (hydrogen bonds and electrostatic complexation). The exhibited "sol–gel" transition based on thermo reversible hydrogen bonds and helical structure reconfiguration facilitated three-dimensional shaping, while strong electrostatic complexation stabilized the evaporator structure. As a proof-of-concept, the 3D-printed evaporator was intrinsically antibacterial and exhibited remarkable swelling resistance (water bath at 100 °C for 14 days, pH = 13) to a harsh water environment and stable solar thermal evaporation (2.3 kg $m^{-2}$ h) under 1 sun irradiation, which was one of the prominent values among the evaporators prepared by direct-ink-writing (DIW).

Received 25th September 2022,
Accepted 6th November 2022

DOI: 10.1039/d2ma00927g

rsc.li/materials-advances



## 1. Introduction

Effective strategies have been proposed to exploit eco-friendly water reclamation technology. Solar-thermal energy is recognized as a sustainable and clean energy, and increasingly novel photothermal materials have been developed for interfacial solar thermal evaporation.[1–4] High hydrophilicity and robust structure of evaporators are generally pivotal for continuous water permeation and evaporation.[5–9] The structure[10,11] and surface properties[12,13] of materials are important for functional applications. Recent research studies have proved that various functional materials and intelligent design structures are instrumental in solar thermal evaporation,[14–16] and three-dimensional structures based on 3D-printing are gradually being developed for more effective photothermal conversion.[17–22] Zheng *et al.*[23] designed a new 3D hydrogel evaporator with hierarchical microstructures, which showed effective thermal insulation to water, while the vertical radial structure ensured water transportation. Liu *et al.*[24] reported a 3D-printed integrated evaporator with a vertical array structure and lattice structures, which were functional for heat collection and water transfer, respectively. Cheng *et al.*[25] prepared a hierarchical micro-nano-porous hydrogel evaporator by 3D layer-by-layer printing, which showed stable photothermal evaporation performance. DIW as one of the simplistic additive manufacturing technologies is suitable for building macroscopic multiscale structures, which has become a promising trend for preparing three-dimensional evaporators recently.

DIW has the advantages of low cost, simple process and wide material applicability, and printing inks generally are non-Newtonian fluids with yield stress, which can form rapidly through extrusion due to the rheological behaviour of shear thinning.[26,27] Conventional dual-network polymers based on DIW were constructed by the synergism of covalent and

[a] State Key Laboratory of Materials Processing and Die & Mold Technology, School of Materials Science and Engineering, Huazhong University of Science and Technology, Wuhan 430074, China. E-mail: roya_wen@hust.edu.cn
[b] Department of Construction Management, School of Civil & Hydraulic Engineering, Huazhong University of Science and Technology, Wuhan 430074, China
[c] Department of Orthopaedics, Union Hospital, Tongji Medical College, Huazhong University of Science and Technology, 430022 Wuhan, China

† Electronic supplementary information (ESI) available. See DOI: https://doi.org/10.1039/d2ma00927g

non-covalent supramolecular interactions, indicating that the precursor inks generally require the addition of reactive monomers, initiators, toxic solvents, *etc.*, for further crosslinking. The integration of 3D printing technology into multiple non-covalently interacting polymers for versatile, structured assemblies is the current focus for developing novel three-dimensional evaporators.

Despite that many polymers based on covalent structural support with intriguing architectures and specific properties have been reported,[27–29] few studies have been reached when it comes to DIW applicable materials with non-covalent supramolecular dual-network design (including host–guest recognition, π–π stacking, hydrogen bonds, hydrophobicity or electrostatic complex) for solar thermal evaporation. Polyelectrolytes with abundant hydrophilic groups (hydroxyl, carboxyl and amino groups, *etc.*) and charge properties are ideal evaporating substrates for building non-covalent supramolecular dual-networks.[30–32] For instance, hydroxyl groups can form a large number of heat-regulatable dynamic hydrogen bonds to meet the fast phase transformation of DIW, while insoluble and refractory electrostatic complexation triggered by oppositely charged groups guaranteed the structural integrity.[33–36] In this dual-network, weaker non-covalent supramolecular interactions were used as "sacrificial bonds", which consumed a lot of energy while breaking, and stronger bonds protected the integrity of the structure after first network breaking.[28,37–42] Polyelectrolytes composed of multiple non-covalent bonds not only match DIW processes but also can expand the range of 3D printable composites.

Here we reported a strategy to construct a non-covalent supramolecular dual-network polyelectrolyte evaporator for stable solar thermal evaporation. CG is a bio-based thermosensitive hydrogel which was chosen as the DIW substrate due to its rapid "sol–gel" phase transition, and this thermally reversible behaviour is owing to the rich hydrogen bonds and helical structure reconfiguration.[43,44] CNT as a rigid filler with a wide range of light absorption effectively improved solar thermal conversion efficiency,[45] and also stabilized hierarchical and porous structures.[23] Further, electrostatic complexation serving as the second crosslinking supramolecular network assured evaporator structural integrity. As a result, reasonable structural design and functional coordination endowed CGP-CNT with remarkable properties such as intrinsic antibacterial activity, thermo and alkali resistance, and exceptional solar thermal evaporation performance among the evaporators prepared by DIW (1 sun irradiation, 2.3 kg $m^{-2}$ h).

## 2. Results and discussion

As shown in Fig. 1, a homogeneous CGP-CNT ink was consecutively extruded by a laboratory DIW printer with a thermostatic sleeve (60 °C), and swift set on the glass substrate attributed to the low-thermal self-gelling property (Fig. S1, ESI†). The interpenetrating condensation of hydrogen bonds and helical reconfiguration lead to the interlayer coalescence without involving volatilization of toxic solvents. Ink concentration and printing process were obtained by further experimental optimization (Fig. S2 and Table S1, ESI†). The formed 3D hydrogel was freeze-dried to remove water, and then soaked in PDADMAC aqueous solution (10 wt%) for further electrostatic complexation. Sulfonic acid groups ($-SO_3^-$) in CG complexed with positive charges in PDADMAC to form a second cross-linking network. It is worth noting that the swelling and complexation should reach a relative kinetic equilibrium in this process, complexation of opposite charges stabilized the polymer microstructure,[46,47] while dilute PADMAC solution may lead to excessive swelling and insufficient complexation of CG-CNT (Fig. S3, ESI†).

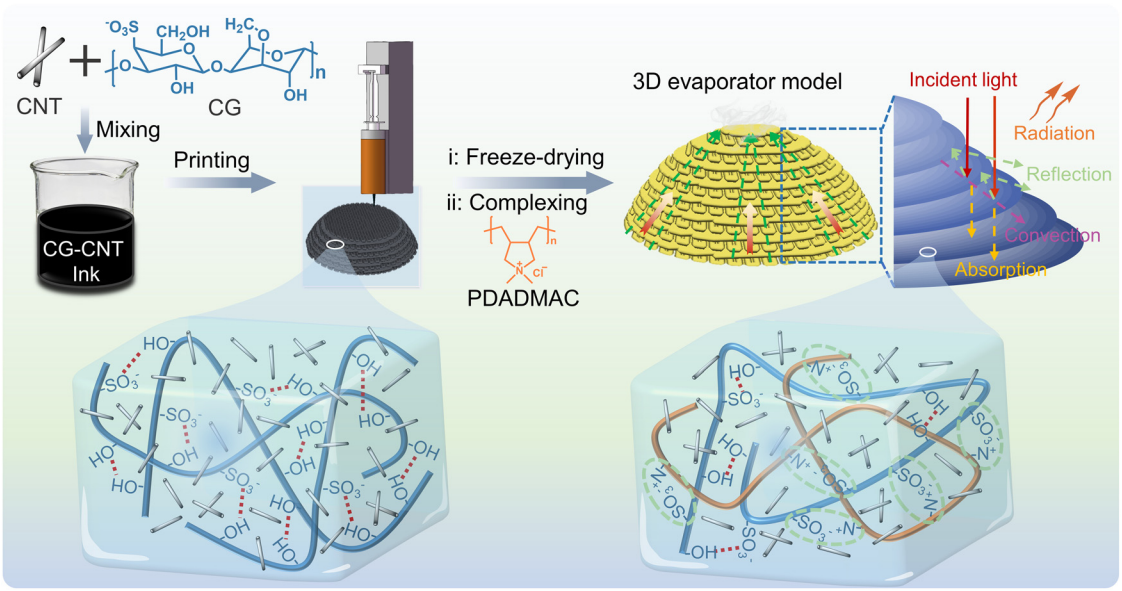


Fig. 1 The preparation of the CGP-CNT evaporator by DIW printing and schematic diagram of the CGP-CNT non-covalent supramolecular dual-network.

Multiple hydrogen bonds endowed CG with thermally reversible behaviour,[48] CG-CNT ink interpenetrated and condensed layer by layer with the assistance of rich hydrogen bonds and helical reconfiguration regulated by thermo difference, and reversible conversion of "sol–gel" also increased composite printability (Movie S1, ESI†). After freeze-drying, CG-CNT complexed with PDADMAC for further cross-linking, and the printed wiring trace was also retained (Fig. S4, ESI†). Firm electrostatic interaction served as a protect key for the structure of the CGP-CNT evaporator, while hydrogen bonds acted as a sacrifice for energy dissipation when it comes to harsh challenges. Relevant literature studies have reported that the three-dimensional stacking construction and the existence of CNT can effectively increase the scattering and absorption of light.[49] The hierarchical structure left on the CGP-CNT surface by DIW was conducive to light absorption.

Continuous ink extrusion was ensured by a thermostatic control device, while gel transition should be fast enough to prevent the ink from depositing on the substrate. Herein, the CG-CNT ink was evaluated by rheological experiments. As shown in Fig. 2a, CG-CNT ink was a gel at low temperature, where storage modulus ($G'$) was higher than loss modulus ($G''$). Then the gel network was gradually destroyed with the increasing temperature, and both $G'$ and $G''$ decreased. When it reached the critical value of about 51 °C, a sudden change occurred ($G' < G''$), while the ink was in a fluid state, which may be conducive to extrusion and shaping. This "sol–gel" transition was a typical rheological behaviour of physical cross-linking networks.[50] The continuous DIW forming process was based on the shear thinning behaviour of CGP-CNT in Fig. 2b. Fast sol–gel transition and narrow gel temperature range allow CG-CNT solutions to be used directly as an ideal three-dimensional forming ink for DIW.

The optical photograph in Fig. 3a showed that the freeze-dried CGP-CNT evaporator can readily stand on the surface of a flexible plant without external disturbance. CNTs were added as a light-absorbing composite and exhibited an excellent photothermal conversion performance. The surface SEM morphology in Fig. 3b showed fine dispersion of CNTs, which were tightly embedded in the CGP matrix, and it was illustrated that CNTs could serve as rigid fillers, which help to stabilize pores during the freeze drying process.[51] As shown in Fig. 3c, the multichannel structure indicated by arrows in CGP-CNT cross-sectional morphology ensured efficient water transmission. Micro-Computed Tomography (Micro-CT) images in Fig. 3d demonstrated the distribution of pores in the CGP-CNT evaporator, and the presence of a polymer network with a porous structure facilitated the continuous water transfer for evaporation.

Fig. 3e shows that CG revealed a characteristic FT-IR peak at 1065 $cm^{-1}$ (blue line), which was assigned to $-SO_3^-$ groups. When compared to CG-CNT, the 1012 $cm^{-1}$ peak can be clearly observed (orange line), which was owing to the quaternary ammonium groups in PDADMAC. This result indicated the complexation of CG and PDADMAC. Tensile strength curves illustrated that the presence of complexation and nanocomposites effectively enhanced the mechanical strength of CGP-CNT (16.6 MPa), when compared to CG-CNT (7.1 MPa) and CGP (9.5 MPa) (Fig. S5, ESI†). Moreover, elemental analysis in Fig. 3f revealed the content changes of nitrogen (N) and sulphur (S) after complexation. Mole ratio (N : S = 1.45) in CGP-CNT increased almost tenfold compared to CG-CNT (0.146), further corroborating the complexation of CG and PDADMAC, and mass content of PDADNMAC in CGP-CNT was 26.3 wt%. EDS analysis showed that both nitrogen and sulphur elements were homogeneously distributed in the CGP-CNT evaporator, respectively, which illustrated the uniformity of complexation. The dynamic contact angle pictures in Fig. 3g showed fast water absorption of the CGP-CNT evaporator, which benefited water transfer for solar thermal evaporation. CGP-CNT was stably formed by two supramolecular dual-networks consisting of hydrogen bonds and electrostatic complexation. The rich polyhydroxy and $-SO_3^-$ groups in CG interactive cross-linked to form a hydrogen bonding network, and $-SO_3^-$ groups complexed with positive charges in PDADMAC to form a second interpenetrating network.

As a proof-of-concept, the utility of CGP-CNT was evaluated by solar thermal tests (Fig. S6, ESI†). As shown in Fig. 4a, high light absorptivity (98%) of wet CGP-CNT was attributed to the fine dispersion of CNTs compared to wet CGP (45%) and multiple reflections of light on the inner graded pores.[52,53] Under 1 sun irradiation, the surface temperature of CGP-CNT (wet) gradually increased to *ca.* 53 °C (Fig. 4b), which was higher than that of CGP (*ca.* 43 °C) and bulk water (*ca.* 38 °C). Infrared images (Fig. S7, ESI†) also confirmed the high-efficiency solar-thermal conversion capability of CGP-CNT. The mass of water decreased linearly with irradiation time, and the evaporation rate of CGP-CNT (2.3 kg $m^{-2}$ h) in Fig. 4c was higher than that of CGP (1.1 kg $m^{-2}$ h) and bulk water (0.8 kg $m^{-2}$ h) under 1 sun irradiation. The hydrophilic groups in CGP-CNT formed hydrogen bonds with water molecules while breaking the hydrogen bonds between free water, thus reducing the energy for evaporation[5,6,54,55] (Fig. S8, ESI†).

The equivalent evaporation enthalpies of water, CGP and CGP-CNT were determined by dark evaporation experiments, which were 2.34, 1.86 and 1.5 kJ $g^{-1}$, respectively (Fig. S9 and S10, ESI†). Further data on the enthalpy of evaporation of the samples were characterised using a differential scanning calorimeter (DSC), which showed that water evaporation enthalpy of

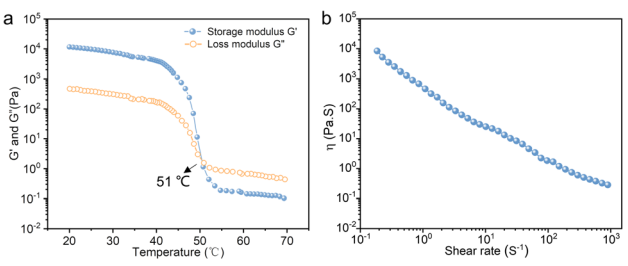


Fig. 2 (a) Storage modulus ($G'$) and loss modulus ($G''$) as a function of temperature for CG-CNT inks at a fixed frequency of 1 Hz. (b) Apparent viscosity as a function of shear rate (0.1–1000 $s^{-1}$) for CG-CNT inks at 60 °C.

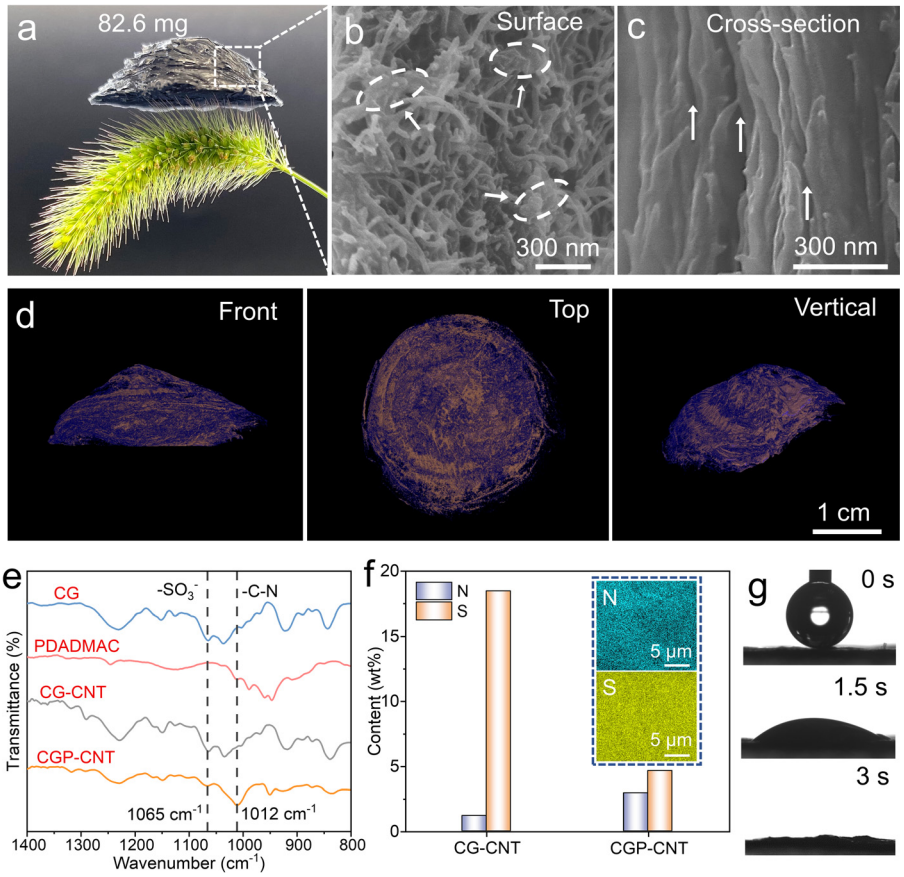


Fig. 3 (a) Photograph exhibiting the light weight of the CGP-CNT evaporator. Surface (b) and cross-section morphologies (c) of CGP-CNT examined by SEM. (d) Micro-CT images of CGP-CNT evaporator from the front, top and vertical sections, respectively (blue part: pore structure; yellow part: polymer) (e) FT-IR curves and (f) element content and EDS analysis of CGP-CNT compared to CG-CNT. (g) Rapid water absorption of CGP-CNT measured by dynamic water contact angle.

CGP-CNT (1.1 kJ $g^{-1}$) reduced by 54% compared to that of bulk water (2.4 kJ $g^{-1}$) (Fig. S11, ESI†). The energy conversion efficiency was calculated by the following equation:

$$\eta = \frac{\Delta v H}{P}$$

where $\eta$ is the energy conversion efficiency, $\Delta v$ is the difference between the evaporation rates under light and dark, $H$ is the water evaporation enthalpy of samples, and $P$ represents the simulated light intensity (1 kW $m^{-2}$).

The effect of evaporator height and CNT content on solar evaporation performance has also been explored (Fig. S12 and S13, ESI†). The charge properties of polyelectrolytes and existence of abundant hydrophilic functional groups were instrumental in absorbing water, while layered pores facilitated water transport. The evaporation rate of CGP-CNT was also one of the prominent values among the evaporators prepared by DIW (Fig. 4d and Table S2, ESI†). The CGP-CNT evaporator possessed extraordinarily heat and swelling resistance (Fig. S14, ESI†), and it remained relatively intact after continuous operation in an alkaline water bath (pH 13) at 100 °C for 14 days (the diameter of the sample only reduced 0.5 cm), which was attributed to the stable electrostatic complexation between strong ions (Fig. 4e). This outstanding feature of resistance to harsh water environments is beyond the reach of many hydrogen bonded solar-thermal materials. FTIR confirmed the structural stability of CGP-CNT after swelling in 100 °C water (Fig. S15, ESI†).

Notably, compared to the performance in other reports,[19,56,57] CGP-CNT exhibited excellent solar thermal evaporation stability in continuous operation (81 h) under different irradiation and water samples. Firstly, as shown in Fig. 5a, the CGP-CNT evaporator was continuously cycled under 1, 3, and 5 sun irradiation for 25 h, and then exposed to the East Lake, Yangtze River, methylene blue, methyl orange, pH 13 and neutral samples for further evaporation tests under one sun irradiation (36 h), successively (Fig. 5b). Optical pictures and UV absorption curves of different water samples after evaporation illustrated the effective purification (Fig. S16, ESI†). As a proof of concept, solar thermal desalination experiment of the CGP-CNT evaporator was operated with real seawater collected from the Bohai Sea (China) for 20 h cycle testing (Fig. 5c). With the increase of test time, salt particles began to crystallize on the surface at the tenth seawater cycle and were obviously enriched at the top of the evaporator by the thirteenth cycle (Fig. S17, ESI†), which led to a rapid decrease in the solar-thermal evaporation rate, consistent

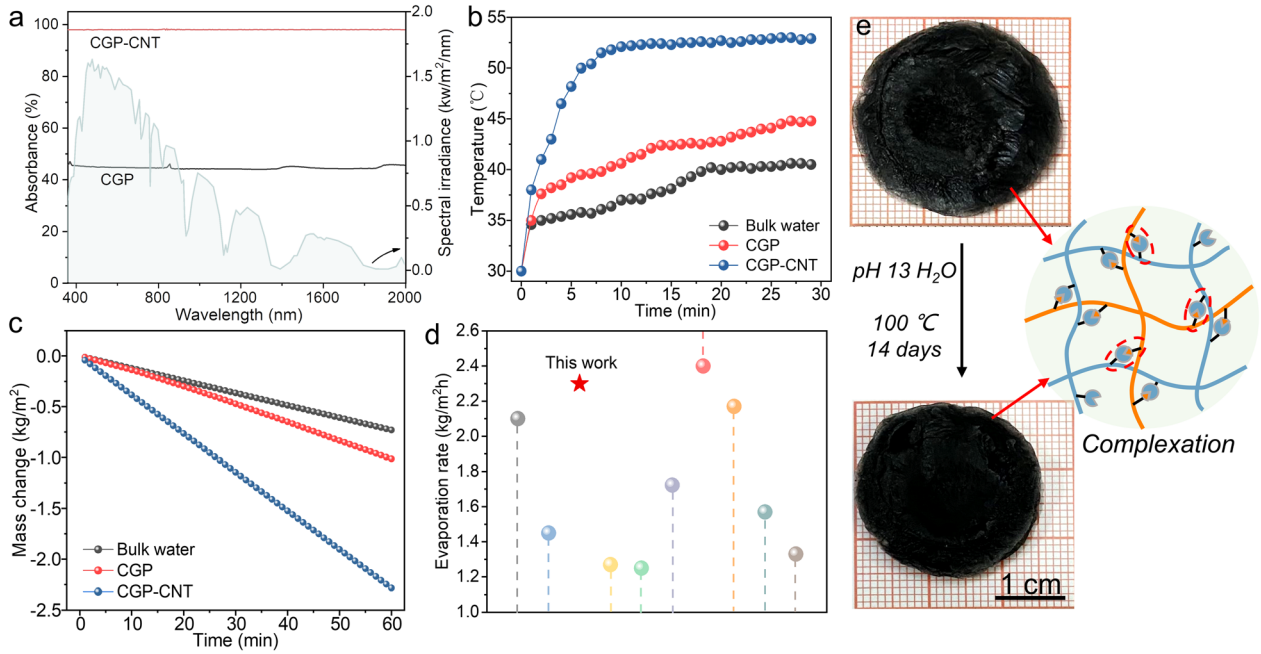


Fig. 4 (a) UV-vis-NIR absorption spectra of wet CGP and CGP-CNT. (b) Surface temperature and (c) evaporation rate of bulk water, CGP and CGP-CNT under 1 kW $m^{-2}$ irradiation. (d) Comparison of the evaporation rate of CGP-CNT with reported 3D photothermal materials by DIW (Table S2, ESI†). (e) Photographs of CGP-CNT after swelling in 100 °C water (pH 13) for 14 days.

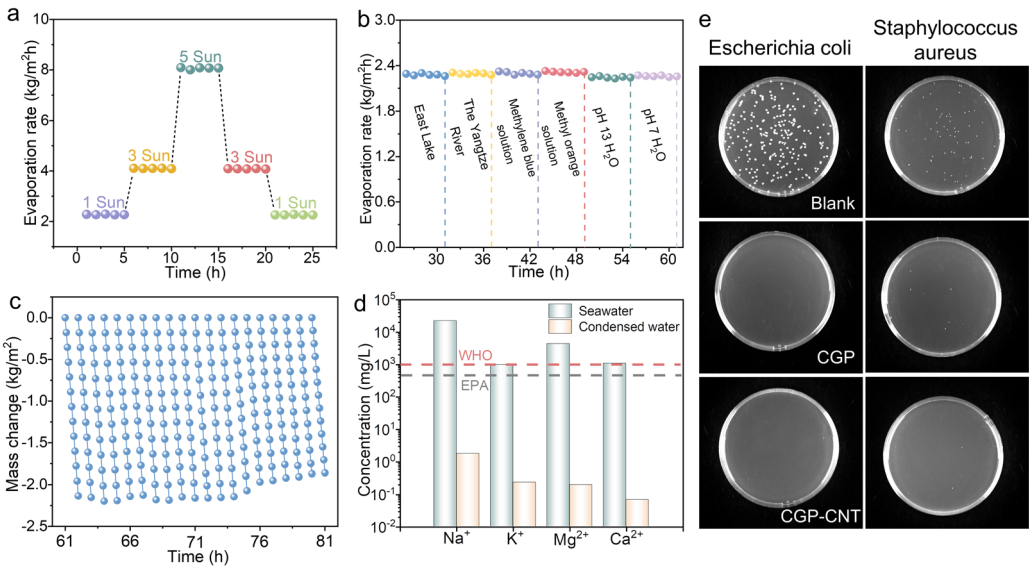


Fig. 5 The evaporation recyclability of CGP-CNT for (a) different sun irradiations, (b) diverse water samples under 1 sun irradiation and (c) seawater under 1 sun irradiation, continuously. (d) Concentration of ions in pristine seawater and the condensed water collected during the solar thermal evaporation of CGP-CNT. (e) Antibacterial properties of CGP and CGP-CNT for *Escherichia coli* and *Staphylococcus aureus*, respectively.

with that reported in the literature.[51,58] Fig. 5d shows that all four primary ions (*i.e.* $Na^+$, $Mg^{2+}$, $K^+$ and $Ca^{2+}$ in condensate water) were 3–4 orders of magnitude lower than pristine seawater and significantly lower than the drinking water standard defined by the World Health Organization (WHO, *i.e.* 1000 mg $L^{-1}$) or the United States Environmental Protection Agency (EPA, *i.e.* 500 mg $L^{-1}$). In this work, the desalination stability of the evaporator in seawater was added as an explored system in cyclic experiments. In the swelling experiment, CGP and CGP-CNT both reached swelling equilibrium (~10 wt%) in real seawater for 11 h, respectively. The mass loss degree of CGP was 10.5 wt%, which was 2.3-fold that of CGP-CNT (4.5 wt%); although rich salt ions in seawater shielded the polyelectrolyte complexation, mass loss of CGP-CNT after swelling was still within an acceptable limit due to

the addition of CNT and hydrogen bonds (Fig. S18 and S19, ESI†). What's more, the CGP-CNT evaporator possessed the intrinsic antibacterial property (Fig. 5e), and guaranteed the purification of different water samples. Compared with the blank group, CGP and CGP-CNT have obvious antibacterial activity on *Escherichia coli* and *Staphylococcus aureus*, which was attributed to quaternary ammonium ions.[59]

# 3. Conclusions

CGP-CNT possessed intrinsic antibacterial, remarkable anti-swelling, and stable solar thermal evaporation performance, and the cost-effective and simple operation based on 3D printing can be applied in additive manufacturing of various functional composites. Layer-by-layer printing processes endowed CGP-CNT with a hierarchical pore structure, while CNTs facilitated solar light absorption and energy conversion. Notably, CGP-CNT has prominent solar thermal evaporation performance under different sun irradiation and water samples for 81 h consecutively (*e.g.*, 2.3 kg $m^{-2}$ h evaporation rate under one sun irradiation) and excellent stability in a harsh water environment; for instance, it can anti-swell cycle for 14 days in aqueous solution (pH = 13, 100 °C). Overall, assembling non-covalent supramolecular dual-networks to meet the 3D printing process and stable solar thermal evaporation, which can be applied to various polyelectrolytes and nano-composites, expands the scope of functional materials accessible by DIW.

# 4. Experimental

### Materials

Poly(diallyldimethylammoniumchloride) ($M_w$ = 400 000–500 000 g $mol^{-1}$, 20 wt% aqueous solution) was purchased from Sigma-Aldrich Industrial Co. Ltd (China). k-Carrageenan, methyl orange and methylene blue were purchased from Aladdin Industrial Co. Ltd (China). CNTs were purchased from Shenzhen nanoport Co. Ltd (China). Sodium hydroxide (NaOH) was purchased from Sinopharm Chemical Reagent Co. Ltd (China).

### Preparation of the CGP-CNT evaporator

Printing ink: 2.04 g of CG and 0.306 g CNT were dissolved in 100 mL $H_2O$, then stirred in a 60 °C water bath (600 rpm) and sonicated for 1 h to form a homogeneous, black CG-CNT ink.

The procedure of DIW:CG-CNT ink was heated to a flowable state in a 60 °C water bath, then transferred to a 5 ml syringe and fixed in the printer (Shangpu Boyuan Biotechnology Co. Ltd China) with a thermal sleeve (60 °C) to ensure continuous extrusion. After extrusion, CGP-CNT ink was solidified layer by layer on a clean glass substrate (room temperature). The computer controlled the printing path, including printing speed, extrusion speed, line distance, layer distance, *etc.*

CGP-CNT evaporator: The printed CG-CNT hydrogel was freeze-dried for 12 h to remove most water, and then swollen in 10 wt% PDADMAC solution (3 h, appropriate ultrasound could be used to accelerate complexation) for enough complexation (Table S3, ESI†). The cross-linked CGP-CNT was washed 3 times with deionized water to remove excess PDADMAC and salts. The method can apply to different composites and polyelectrolyte complexation systems (Fig. S20, ESI†).

### Solar thermal evaporation experiments

A solar light simulator (CEL-S500L) was used to conduct the solar thermal steaming measurement at *ca.* 35 ± 1 °C room temperature and 35 ± 1% relative humidity. The evaporator was placed on the surface of PS foam covered with hydrophilic cotton, which effectively prevented the heat from transferring to water, and hydrophilic cotton also ensured the transport of water. Seawater for solar thermal tests was collected from the Bohai Sea (China). Surface temperature of samples was monitored using an infrared camera. An electronic balance (JA2003, Soptop) was used for recording water mass changes. The evaporator sample was a three-dimensional cone-shaped porous aerogel, approximately 3 cm in diameter and 1 cm in height, respectively. The evaporation rate $R$ (kg $m^{-2}$ h) was calculated by the following equation:

$$R = m/(s \cdot t)$$

$$S = \pi \cdot r \cdot 1$$

where $m$ represents the mass change of water under 1 sun irradiation, $s$ is the sample area ($m^2$), and $t$ denotes the solar irradiation time. $r$ is the radius of the circle at the base of the cone, and $l$ is the length of the bus bar of the cone. (Note: Due to the slightly deformed shape of the evaporator after freeze-drying, the effective photothermal area was calculated according to the conical side area of the experimental sample.)

The swelling degree (SD) was calculated using the following equation:

$$\mathrm{SD} = 100\% \cdot (m_1 - m_0)/m_0$$

where $m_1$ represents the sample swelling equilibrium mass and $m_0$ is the initial mass of the dried sample.

### Characterization

The morphologies of CGP-CNT were observed by electron microscopy (FESEM, Hitachi, SU-8010). Fourier transform infrared spectroscopy (FT-IR) was performed using a BRUKER Vertex 80 FT-IR. The dynamic water contact angle was measured using a contact angle meter (DATAPPHYSICS, OCA20). Element analyses (C, N, S and H) were performed using an element analyzer (PERKIN ELMER, Optima 5300-DV). The absorption spectrum, pore distribution and mechanical property for CGP-CNT were measured using a UV-Vis-NIR spectrophotometer (PerkinElmer, Lambda 750S), Micro-CT (GE, Vtomex) and electronic universal testing machine (Sansi, SHT4206), respectively. The rheological properties were analyzed using a rheometer (TA, DHR-2). Ion contents were measured using an inductively coupled plasma emission spectrometer (ICP-OES, PerkinElmer 8300). pH values were measured using a digital pH meter (SARTORIUS, PB-10).

## Author contributions

Shifeng Wen, Bin Su and Yan Zhou designed the experimental project. Sihan Tang performed the experiments and analysed the data. Sihan Tang wrote the paper. All the authors discussed and interpreted the results.

## Conflicts of interest

There are no conflicts to declare.

## Acknowledgements

This work was supported by the National Natural Science Foundation of China (NSFC) (Grant No. U1808216, 52105296, 52105339). S. H., S. F., and B. S. supervised the project. S. H. is responsible for experiments and grateful to J. S. for providing the DIW printer. All authors wrote the work.

## Notes and references

1 L. Wu, Z. Dong, Z. Cai, T. Ganapathy, N. X. Fang, C. Li, C. Yu, Y. Zhang and Y. Song, *Nat. Commun.*, 2020, **11**, 521.
2 Y. Shi, O. Ilic, H. A. Atwater and J. R. Greer, *Nat. Commun.*, 2021, **12**, 2797.
3 J. Li, X. Wang, Z. Lin, N. Xu, X. Li, J. Liang, W. Zhao, R. Lin, B. Zhu, G. Liu, L. Zhou, S. Zhu and J. Zhu, *Joule*, 2020, **4**, 928–937.
4 Y. Guo, X. Zhao, F. Zhao, Z. Jiao, X. Zhou and G. Yu, *Energy Environ. Sci.*, 2020, **13**, 2087–2095.
5 F. Zhao, X. Zhou, Y. Shi, X. Qian, M. Alexander, X. Zhao, S. Mendez, R. Yang, L. Qu and G. Yu, *Nat. Nanotechnol.*, 2018, **13**, 489–495.
6 F. Zhao, Y. Guo, X. Zhou, W. Shi and G. Yu, *Nat. Rev. Mater.*, 2020, **5**, 388–401.
7 Y. Xia, Q. Hou, H. Jubaer, Y. Li, Y. Kang, S. Yuan, H. Liu, M. W. Woo, L. Zhang, L. Gao, H. Wang and X. Zhang, *Energy Environ. Sci.*, 2019, **12**, 1840–1847.
8 F. Zhao, X. Zhou, Y. Guo, B. Rosenberger and G. Yu, *Sci. Adv.*, 2019, **5**, eaaw5484.
9 Y. Shi, R. Li, Y. Jin, S. Zhuo, L. Shi, J. Chang, S. Hong, K.-C. Ng and P. Wang, *Joule*, 2018, **2**, 1171–1186.
10 X. Zhang, Q. Wang, R. Zou, B. Song, C. Yan, Y. Shi and B. Su, *Engineering*, 2022, **15**, 196–205.
11 Z. Ma, Q. Wang, Z. Wu, D. Chen, C. Yan, Y. Shi, M. D. Dickey and B. Su, *Adv. Mater.*, 2022, **34**, e2203814.
12 Z. Wu, H. Sun, Z. Xu, H. Chi, X. Li, S. Wang, T. Zhang and Y. Zhao, *ACS Appl. Nano Mater.*, 2021, **4**, 8979–8989.
13 H. Chi, Z. Xu, Z. Wei, T. Zhang, H. Wang, T. Lin and Y. Zhao, *ACS Appl. Mater. Interfaces*, 2021, **13**, 29150–29157.
14 P. Wu, X. Wu, H. Xu and G. Owens, *EcoMat*, 2021, **3**, e12140.
15 Y. Wang, X. Wu, P. Wu, J. Zhao, X. Yang, G. Owens and H. Xu, *Sci. Bull.*, 2021, **66**, 2479–2488.
16 Y. Wang, X. Wu, P. Wu, H. Yu, J. Zhao, X. Yang, Q. Li, Z. Zhang, D. Zhang, G. Owens and H. Xu, *J. Mater. Chem. A*, 2022, **10**, 14470–14478.
17 Y. Wang, X. Wu, T. Gao, Y. Lu, X. Yang, G. Y. Chen, G. Owens and H. Xu, *Nano Energy*, 2021, **79**, 105477.
18 Z. Wang, W. Tu, Y. Zhao, H. Wang, H. Huang, Y. Liu, M. Shao, B. Yao and Z. Kang, *J. Mater. Chem. A*, 2020, **8**, 14566–14573.
19 S. Zhou, S. Huang, Y. Ming, Y. Long, H. Liang, S. Ruan, Y.-J. Zeng and H. Cui, *J. Mater. Chem. A*, 2021, **9**, 9909–9917.
20 M. Zou, Y. Zhang, Z. Cai, C. Li, Z. Sun, C. Yu, Z. Dong, L. Wu and Y. Song, *Adv. Mater.*, 2021, **33**, e2102443.
21 T. Gao, X. Wu, Y. Wang, G. Owens and H. Xu, *Sol. RRL*, 2021, **5**, 2100053.
22 Y. Lu, D. Fan, Z. Shen, H. Zhang, H. Xu and X. Yang, *Nano Energy*, 2022, **95**, 107016.
23 X. Liu, F. Chen, Y. Li, H. Jiang, D. D. Mishra, F. Yu, Z. Chen, C. Hu, Y. Chen, L. Qu and W. Zheng, *Adv. Mater.*, 2022, e2203137.
24 Y. Yang, W. Fan, S. Yuan, J. Tian, G. Chao and T. Liu, *J. Mater. Chem. A*, 2021, **9**, 23968–23976.
25 J. Yuan, X. Lei, C. Yi, H. Jiang, F. Liu and G. J. Cheng, *Chem. Eng. J.*, 2022, **430**, 132765.
26 X. Li, H. Wang, D. Li, S. Long, G. Zhang and Z. Wu, *ACS Appl. Mater. Interfaces*, 2018, **10**, 31198–31207.
27 F. Zhu, L. Cheng, J. Yin, Z. L. Wu, J. Qian, J. Fu and Q. Zheng, *ACS Appl. Mater. Interfaces*, 2016, **8**, 31304–31310.
28 H. Li, C. Tan and L. Li, *Mater. Des.*, 2018, **159**, 20–38.
29 H. Yang, C. Li, M. Yang, Y. Pan, Q. Yin, J. Tang, H. J. Qi and Z. Suo, *Adv. Funct. Mater.*, 2019, 1901721.
30 Z. Chen, D. Zhao, B. Liu, G. Nian, X. Li, J. Yin, S. Qu and W. Yang, *Adv. Funct. Mater.*, 2019, **29**, 1900971.
31 D. Chimene, R. Kaunas and A. K. Gaharwar, *Adv. Mater.*, 2020, **32**, e1902026.
32 Y. Zhou, M. Layani, S. Wang, P. Hu, Y. Ke, S. Magdassi and Y. Long, *Adv. Funct. Mater.*, 2018, **28**, 1705365.
33 F. Luo, T. L. Sun, T. Nakajima, T. Kurokawa, Y. Zhao, K. Sato, A. B. Ihsan, X. Li, H. Guo and J. P. Gong, *Adv. Mater.*, 2015, **27**, 2722–2727.
34 P. Schaaf and J. B. Schlenoff, *Adv. Mater.*, 2015, **27**, 2420–2432.
35 H. C. Yu, S. Y. Zheng, L. Fang, Z. Ying, M. Du, J. Wang, K. F. Ren, Z. L. Wu and Q. Zheng, *Adv. Mater.*, 2020, **32**, e2005171.
36 M. J. Yin, Q. Zhao, J. Wu, K. Seefeldt and J. Yuan, *ACS Nano*, 2018, **12**, 12551–12557.
37 Z. Bao, C. Xian, Q. Yuan, G. Liu and J. Wu, *Adv. Healthcare Mater.*, 2019, **8**, e1900670.
38 M. A. Darabi, A. Khosrozadeh, R. Mbeleck, Y. Liu, Q. Chang, J. Jiang, J. Cai, Q. Wang, G. Luo and M. Xing, *Adv. Mater.*, 2017, **29**, 1700533.
39 F. Gao, Z. Xu, Q. Liang, B. Liu, H. Li, Y. Wu, Y. Zhang, Z. Lin, M. Wu, C. Ruan and W. Liu, *Adv. Funct. Mater.*, 2018, **28**, 1706644.
40 D. L. Taylor and M. In Het Panhuis, *Adv. Mater.*, 2016, **28**, 9060–9093.
41 S. Van Belleghem, L. Torres, Jr., M. Santoro, B. Mahadik, A. Wolfand, P. Kofinas and J. P. Fisher, *Adv. Funct. Mater.*, 2020, **30**, 1907145.

42 Y. Wang, Q. Chang, R. Zhan, K. Xu, Y. Wang, X. Zhang, B. Li, G. Luo, M. Xing and W. Zhong, *J. Mater. Chem. A*, 2019, **7**, 24814–24829.
43 S. Liu and L. Li, *ACS Appl. Mater. Interfaces*, 2017, **9**, 26429–26437.
44 D. J. Adams, *J. Am. Chem. Soc.*, 2022, **144**, 11047–11053.
45 Y. Ni, X. Zhou, J. Gong, L. Xue and Q. Zhao, *Adv. Funct. Mater.*, 2021, **31**, 2103818.
46 C. F. J. Faul and M. Antonietti, *Adv. Mater.*, 2003, **15**, 673–683.
47 L. Li, A. M. Rumyantsev, S. Srivastava, S. Meng, J. J. de Pablo and M. V. Tirrell, *Macromolecules*, 2020, **54**, 105–114.
48 L. Li, B. Yan, J. Yang, L. Chen and H. Zeng, *Adv. Mater.*, 2015, **27**, 1294–1299.
49 Y. Qiao, S. Xu, T. Zhu, N. Tang, X. Bai and C. Zheng, *Polymer*, 2020, **186**, 121994.
50 S. Hietala, P. Mononen, S. Strandman, P. Järvi, M. Torkkeli, K. Jankova, S. Hvilsted and H. Tenhu, *Polymer*, 2007, **48**, 4087–4096.
51 F. Guo, Y. Jiang, Z. Xu, Y. Xiao, B. Fang, Y. Liu, W. Gao, P. Zhao, H. Wang and C. Gao, *Nat. Commun.*, 2018, **9**, 881.
52 Y. Li, X. Cui, M. Zhao, Y. Xu, L. Chen, Z. Cao, S. Yang and Y. Wang, *J. Mater. Chem. A*, 2019, **7**, 704–710.
53 D.-D. Qin, Y.-J. Zhu, F.-F. Chen, R.-L. Yang and Z.-C. Xiong, *Carbon*, 2019, **150**, 233–243.
54 N. Liu, L. Hao, B. Zhang, R. Niu, J. Gong and T. Tang, *Energy Environ. Mater.*, 2021, **5**, 1–10.
55 H. Bai, N. Liu, L. Hao, P. He, C. Ma, R. Niu, J. Gong and T. Tang, *Energy Environ. Mater.*, 2021, **0**, 1–10.
56 Z. Wang, H. Liu, F. Chen and Q. Zhang, *J. Mater. Chem. A*, 2020, **8**, 19387–19395.
57 X. Ming, A. Guo, Q. Zhang, Z. Guo, F. Yu, B. Hou, Y. Wang, K. P. Homewood and X. Wang, *Carbon*, 2020, **167**, 285–295.
58 N. Cao, S. Lu, R. Yao, C. Liu, Q. Xiong, W. Qin and X. Wu, *Chem. Eng. J.*, 2020, **397**, 125522.
59 A. Jain, L. S. Duvvuri, S. Farah, N. Beyth, A. J. Domb and W. Khan, *Adv. Healthcare Mater.*, 2014, **3**, 1969–1985.